

# Search for Higgs Bosons in SUSY Cascades in CMS and Dark Matter with Non-universal Gaugino Masses

Katri Huitu<sup>1,2,a</sup>, Ritva Kinnunen<sup>1,b</sup>, Jari Laamanen<sup>3,1,c</sup>, Sami Lehti<sup>1,d</sup>, Sourov Roy<sup>4,e</sup>, and Tapio Salminen<sup>2,f</sup>

<sup>1</sup> Helsinki Institute of Physics, P.O. Box 64, FIN-00014 University of Helsinki, Finland

<sup>2</sup> Department of Physics, P.O. Box 64, FIN-00014 University of Helsinki, Finland

<sup>3</sup> Institut für Physik, Technische Universität Dortmund, D-44221 Dortmund, Germany

<sup>4</sup> Department of Theoretical Physics and Centre for Theoretical Sciences,  
Indian Association for the Cultivation of Science, 2A & 2B Raja S.C. Mullick Road, Kolkata 700 032, India

**Abstract.** In grand unified theories (GUT), non-universal boundary conditions for the gaugino masses may arise at the unification scale, and affect the observability of the neutral MSSM Higgs bosons ( $h/H/A$ ) at the LHC. The implications of such non-universal gaugino masses are investigated for the Higgs boson production in the SUSY cascade decay chain  $\tilde{g} \rightarrow \tilde{q}q$ ,  $\tilde{q} \rightarrow \tilde{\chi}_2 q$ ,  $\tilde{\chi}_2 \rightarrow \tilde{\chi}_1 h/H/A$ ,  $h/H/A \rightarrow b\bar{b}$  produced in pp interactions. In the singlet representation with universal gaugino masses only the light Higgs boson can be produced in this cascade with the parameter region of interest for us, while with non-universal gaugino masses heavy neutral MSSM Higgs boson production may dominate. The allowed parameter space in the light of the WMAP constraints on the cold dark matter relic density is investigated in the above scenarios for gaugino mass parameters. We also demonstrate that combination of representations can give the required amount of dark matter in any point of the parameter space. In the non-universal case we show that heavy Higgs bosons can be detected in the studied cascade in parameter regions with the WMAP preferred neutralino relic density.

**PACS.** 12.60.Jv Supersymmetric models – 95.35.+d Dark matter – 14.80.Cp Non-standard-model Higgs bosons – 14.80.Ly Supersymmetric partners of known particles – 12.10.Kt Unification of couplings; mass relations

## 1 Introduction

Most studies concerning the discovery potential for finding supersymmetric Higgs bosons at the LHC, have been done in models with universal gaugino masses at the unification scale. There is, however, no compelling theoretical reason for such a choice. In grand unified supersymmetric models, which include an SU(5) grand unified model, non-universal gaugino masses are generated by a nonsinglet chiral superfield  $\Phi^n$  that appears linearly in the gauge kinetic function  $f(\Phi)$ . The function  $f(\Phi)$  is an analytic function of the chiral superfields  $\Phi$  in the theory [1]. It should be noted that the chiral superfields  $\Phi$  consist of a set of gauge singlet superfields  $\Phi^s$  and gauge nonsinglet superfields  $\Phi^n$ , respectively, under the grand unified group. If the auxiliary part  $F_\Phi$  of a chiral superfield  $\Phi$  in the  $f(\Phi)$  gets a VEV, then gaugino masses arise from the

coupling of  $f(\Phi)$  with the field strength superfield  $W^a$ . The Lagrangian for the coupling of gauge kinetic function with the gauge field strength is written as

$$\mathcal{L}_{gk} = \int d^2\theta f_{ab}(\Phi) W^a W^b + H.c. \quad (1)$$

where  $a$  and  $b$  are gauge group indices [for example,  $a, b = 1, 2, \dots, 24$  for SU(5)], and repeated indices are summed over. The gauge kinetic function  $f_{ab}(\Phi)$  is

$$f_{ab}(\Phi) = f_0(\Phi^s)\delta_{ab} + \sum_n f_n(\Phi^s) \frac{\Phi^n_{ab}}{M_P} + \dots, \quad (2)$$

where as described above the  $\Phi^s$  and  $\Phi^n$  are the singlet and nonsinglet chiral superfields, respectively. Here  $f_0(\Phi^s)$  and  $f_n(\Phi^s)$  are functions of gauge singlet superfields  $\Phi^s$ , and  $M_P$  is some large scale. When  $F_\Phi$  gets a VEV  $\langle F_\Phi \rangle$ , the interaction (1) gives rise to gaugino masses:

$$\mathcal{L}_{gk} \supset \frac{\langle F_\Phi \rangle_{ab}}{M_P} \lambda^a \lambda^b + H.c., \quad (3)$$

where  $\lambda^{a,b}$  are gaugino fields. It should be noted that the U(1), SU(2), and SU(3) gauginos are denoted by  $\lambda_1$ ,  $\lambda_2$ , and  $\lambda_3$ , respectively.

<sup>a</sup> katri.huitu@helsinki.fi

<sup>b</sup> ritva.kinnunen@helsinki.fi

<sup>c</sup> jari.laamanen@uni-dortmund.de

<sup>d</sup> sami.lehti@helsinki.fi

<sup>e</sup> tpsr@iacs.res.in

<sup>f</sup> Tapio.Salminen@helsinki.fi

Since the gauginos belong to the adjoint representation of the gauge group, in the case of SU(5) for example,  $\Phi$  and  $F_\Phi$  can belong to any of the following representations appearing in the symmetric product of the two **24** dimensional representations of SU(5):

$$(\mathbf{24} \otimes \mathbf{24})_{\text{Symm}} = \mathbf{1} \oplus \mathbf{24} \oplus \mathbf{75} \oplus \mathbf{200}. \quad (4)$$

In the minimal case (which is the simplest one too),  $\Phi$  and  $F_\Phi$  are assumed to be in the singlet representation of SU(5). This corresponds to equal gaugino masses at the GUT scale. However,  $\Phi$  can belong to any of the nonsinglet representations **24**, **75**, and **200** of SU(5). In that case, the gaugino masses are unequal but related to one another via the representation invariants [2, 3, 4]. It should be kept in mind that an arbitrary combination of these different representations is also allowed. We shall first study the case of each representation separately, and then the effect of combining two of these. In Table 1 we display the ratios of resulting gaugino masses at tree level as they arise when  $F_\Phi$  belongs to various representations of SU(5). Clearly, the nonsinglet representations have characteristic mass relationships for the gauginos at the GUT scale. The resulting relations at the electroweak scale, using the renormalization group (RG) evolution at the one-loop level are also displayed.

Table 1: Ratios of gaugino mass parameters at the GUT scale in the normalization  $M_3(\text{GUT}) = 1$  and at the electroweak scale in the normalization  $M_3(\text{EW}) = 1$  at the one-loop level.

$F_\Phi$	$M_1^G$	$M_2^G$	$M_3^G$	$M_1^{\text{EW}}$	$M_2^{\text{EW}}$	$M_3^{\text{EW}}$
<b>1</b>	1	1	1	0.14	0.29	1
<b>24</b>	-0.5	-1.5	1	-0.07	-0.43	1
<b>75</b>	-5	3	1	-0.72	0.87	1
<b>200</b>	10	2	1	1.44	0.58	1

The phenomenology of supersymmetric models with nonuniversal gaugino masses has been considered e.g. in [5, 6, 7, 8, 9, 10, 11, 12]. Studies were performed also in the context of supersymmetric dark matter [13, 14, 15, 16, 17, 18, 19]. The phenomenology of supersymmetric models depends crucially on the compositions of neutralinos and charginos. Hence, it is extremely important to investigate the changes in the experimental signatures with the changes in the composition of neutralinos and charginos which arise because of the non-universal gaugino masses at the GUT scale. In this study our focus will be on the experimental signatures of neutral Higgs bosons appearing in the cascade decay chains of the squark and gluinos produced at the LHC. If the squarks and gluinos are light enough, their production cross sections are large at the LHC. The light neutralinos  $\tilde{\chi}_{1,2}$  are typical decay products of  $\tilde{g}$  and  $\tilde{q}$ . The neutral Higgs bosons can be produced in the decay of  $\tilde{\chi}_2$ , if the mass difference between  $\tilde{\chi}_2$  and  $\tilde{\chi}_1$  is large enough. As the production rate is largely independent of the value of  $\tan\beta$ , these production channels

have been found particularly interesting at the LHC to cover the difficult region of low and medium  $\tan\beta$  values [20, 21]. Production of Higgs via  $\tilde{\chi}_2 \rightarrow \tilde{\chi}_1 h/H/A$  in models where gauginos are in singlet and **24** representation were studied in [5]. Also, recently the role of gaugino mass non-universality (in a model independent framework) in the context of Higgs productions has been discussed in [22]. It was found for sample parameters that only the lightest Higgs could be produced in the model with singlet, while also the heavy Higgses, H and A, could be produced from the cascade in the model with **24** representation. The gaugino mass parameters indeed indicate that it is more probable to have the cascade decay including heavy Higgses in the model with gauginos in **24**. Namely, if the  $\mu$  parameter, mixing Higgs superfields in the MSSM superpotential, is large, the lightest neutralino using either representations is close to bino, while the second lightest is close to wino. From Table 1, in the model with singlet the mass difference of the neutralinos is then close to the mass of the lightest neutralino, since  $m_{\tilde{\chi}_2} \simeq 2m_{\tilde{\chi}_1}$ , while in the model with **24**,  $m_{\tilde{\chi}_2} \simeq 6m_{\tilde{\chi}_1}$  and the mass difference thus five times the mass of the lightest neutralino. Note that the cascade is not possible with small values of the  $\mu$ -parameter, since in such a case  $\tilde{\chi}_2$  and  $\tilde{\chi}_1$  are similar in mass. From Table 1, one can also note that the cascade in the cases of representation **75** is not probable.

In this work, the Higgs boson decay to b quarks,  $H/A/h \rightarrow b\bar{b}$ , with a large branching fraction ( $\sim 0.9$ ) is selected. In the multi-jet events this decay mode suffers from a large combinatorial background, but structuring the event into two hemispheres according to the directions of the decaying gluinos and squarks from the hard process, this background can be efficiently reduced. Production of the light Higgs boson h in SUSY cascades with  $b\bar{b}$  final state has been studied in [23] in the CMS detector with the assumption of universal gaugino masses. The event selection is based on a requirement of four energetic jets, large missing  $E_T$ , separation of the jets into two hemispheres and the reconstruction of the Higgs boson mass from two jets tagged as b jets. Similar analysis method is used here. The main phenomenological differences between approaches of Ref. [23] and this work are the different branching fractions of the SUSY particles. In the singlet representation only the light Higgs boson h can be produced whereas in the representation **24** the  $\tilde{\chi}_2 \rightarrow H/A\tilde{\chi}_1$  decays dominate in most of the parameter space. Therefore considerable differences can be expected in the final mass distribution as well as the obtainable significance of the signal. In Ref. [5] the  $4b$  final state from  $H/A/h \rightarrow b\bar{b}$  decay from both of the cascades has been proposed as the search channel. This mode however is subject to a large combinatorial background from  $b\bar{b}$  combinations due to real or fake b jets in the cascade not containing the Higgs boson.

Combining information from different sources is essential for utilizing future facilities in best possible way. In addition to the laboratory studies, relevant input is obtained from the dark matter searches: the WMAP satellite has put precise limits on the relic density. Supersymmetric

theories which preserve  $R$  parity contain a natural candidate for the cold dark matter particle. If the lightest neutralino is the lightest supersymmetric particle (LSP), it can provide the appropriate relic density. In many SUGRA type models the lightest neutralino is bino-like, which often leads to too large thermal relic density, as compared to the limits provided by the WMAP experiment [24, 25]. Of the possible representations of SU(5) GUT all but the singlet representation produce nonuniversal gaugino masses. Thus the resulting neutralino composition changes from the usual universal gaugino mass case [5]. Depending on the representation where the gauginos are, this leads to different regions in the parameter space where WMAP constraints are satisfied. It is also shown that by combining representations, observationally allowed dark matter parameter regions are not very restricted, if parameters are suitably chosen.

Here we are interested in the case when both the relic density constraints from WMAP can be satisfied and the heavy Higgses can be produced in the cascade. An important contribution to the neutralino annihilation comes from the enhancement due to the Higgs resonance. If we denote the mass of the heavy Higgs, either H or A, by  $m_A$ , the enhanced annihilation occurs when  $m_{\tilde{\chi}_1} = 0.5m_A$ . Since the mass difference between the two lightest neutralinos is  $0.5m_A$  in the model with singlet and  $2.5m_A$  in the model with **24**, it is obvious that this mechanism is available in the latter case, but not in the case with singlet, if we want to study the Higgs production via cascade at the same time. Indeed, we find easily parameter sets with both neutralino dark matter and the cascade to all the Higgses h, H, and A in the model with **24** but not in the model with singlet. Thus in this work we are especially interested in the model with representation **24**, for which also the production cross sections for heavy Higgses were found reasonably large in [5]. In order to have both relevant region for dark matter and to produce heavy Higgses in the cascade decays, the model with **24** is special among those with nonuniversal SU(5) representations. We shall see later that in the model with **200**, the relic density is never large enough to produce the dark matter solely. In **75** the mass difference between the two lightest neutralinos is too small for the cascade decay in the parameter region with relic density in the WMAP region.

In the following we first discuss in section 2 the parameter regions for observationally acceptable dark matter in different SU(5) representations. In section 3 we concentrate on representation **24** and specifically study the parameter region, where the Higgs production from neutralino decay is most promising, and the signal and background processes are discussed. The detector simulation is shortly presented in Section 4. The event selection and the signal to background ratio are discussed in Section 5, and the background determination is elaborated in Section 6. Section 7 describes the systematic uncertainties on the background determination. Discovery potential is given in Section 8 and the conclusions in Section 9.

## 2 Dark matter in SU(5) representations

We start the description of the relic density for four different SU(5) representations with the representation **24**, which is most interesting for us here, as explained in the introduction. We then shortly discuss the representations **75** and **200**, and compare with the singlet, which has been studied extensively in the literature. Then we discuss combination of singlet representation with **200**.

The amount of thermal relic density in the representation **24** is presented in Fig. 1 for four different sets of GUT scale parameters. The spectrum was calculated with SOFTSUSY [26] and relic densities and constraints with micrOMEGAs [27, 28, 29]. The dark shaded areas represent larger relic density than the lighter areas. For the relic density, we use here the WMAP combined three year limits [24, 25]

$$\Omega_{CDM}h^2 = 0.11054^{+0.00976}_{-0.00956} \quad (2\sigma). \quad (5)$$

For the particle masses, the following limits are applied [29]:  $m_{\tilde{e}_R} > 99.4$  or  $100.5$  GeV depending if the lightest neutralino mass is below or above 40 GeV,  $m_{\tilde{\mu}_R} > 95$  GeV,  $m_{\tilde{\tau}_1} > 80.5$  to 88 GeV depending on the lightest neutralino mass (from 10 to 75 GeV),  $m_{\tilde{\nu}_i} > 43$  GeV, and  $m_{\tilde{\chi}^\pm} > 73.1$  to 103 GeV depending on the sneutrino masses (from 45 to 425 GeV). The curve  $m_h = 114$  GeV is depicted in the figure. For the shown parameter region, when otherwise experimentally allowed, Higgs is always heavier than 91 GeV, which is the Higgs mass limit in MSSM for  $\tan\beta \geq 10$  assuming maximal top mixing [30].

The most striking feature in Fig. 1 is the valley of the low relic density area around  $M_2 \sim -300$  GeV. There the annihilation of neutralinos proceeds to quarks and the minimum occurs at the  $Z$  peak providing an efficient annihilation. Outside of the valley the relic density rises, overclosing the universe. In the representation **24** the lightest neutralino is very bino-like, and the WMAP preferred region tends to be quite narrow.

If the overall relic density is low, the crucial differences that control the preferred regions of the parameter space come mostly from the composition of the lightest neutralino. An important single aspect that separates the different parameter sets in Fig. 1 is the presence of the higgsino component in the lightest neutralino, which increases annihilation into the gauge boson pairs. Increasing the value of  $\tan\beta$  decreases the value of the supersymmetric higgsino mass parameter  $\mu$ , as can be seen from the electroweak symmetry breaking (EWSB) condition

$$|\mu|^2 = \frac{m_{H_d}^2 - m_{H_u}^2 \tan^2 \beta}{\tan^2 \beta - 1} - \frac{1}{2}m_Z^2, \quad (6)$$

where  $\tan\beta \equiv \langle H_u^0 \rangle / \langle H_d^0 \rangle = v_u / v_d$ . This results in a bigger higgsino component in the lightest neutralino, which then annihilates more efficiently. The effect is seen in comparing Figures 1a and 1b. Since the relic density in Fig. 1b is smaller than in Fig. 1a in general, also annihilation to the lightest Higgs suffices to lower the relic density to the WMAP preferred region. Thus the low relic density region is wider than in Fig. 1a with bands corresponding

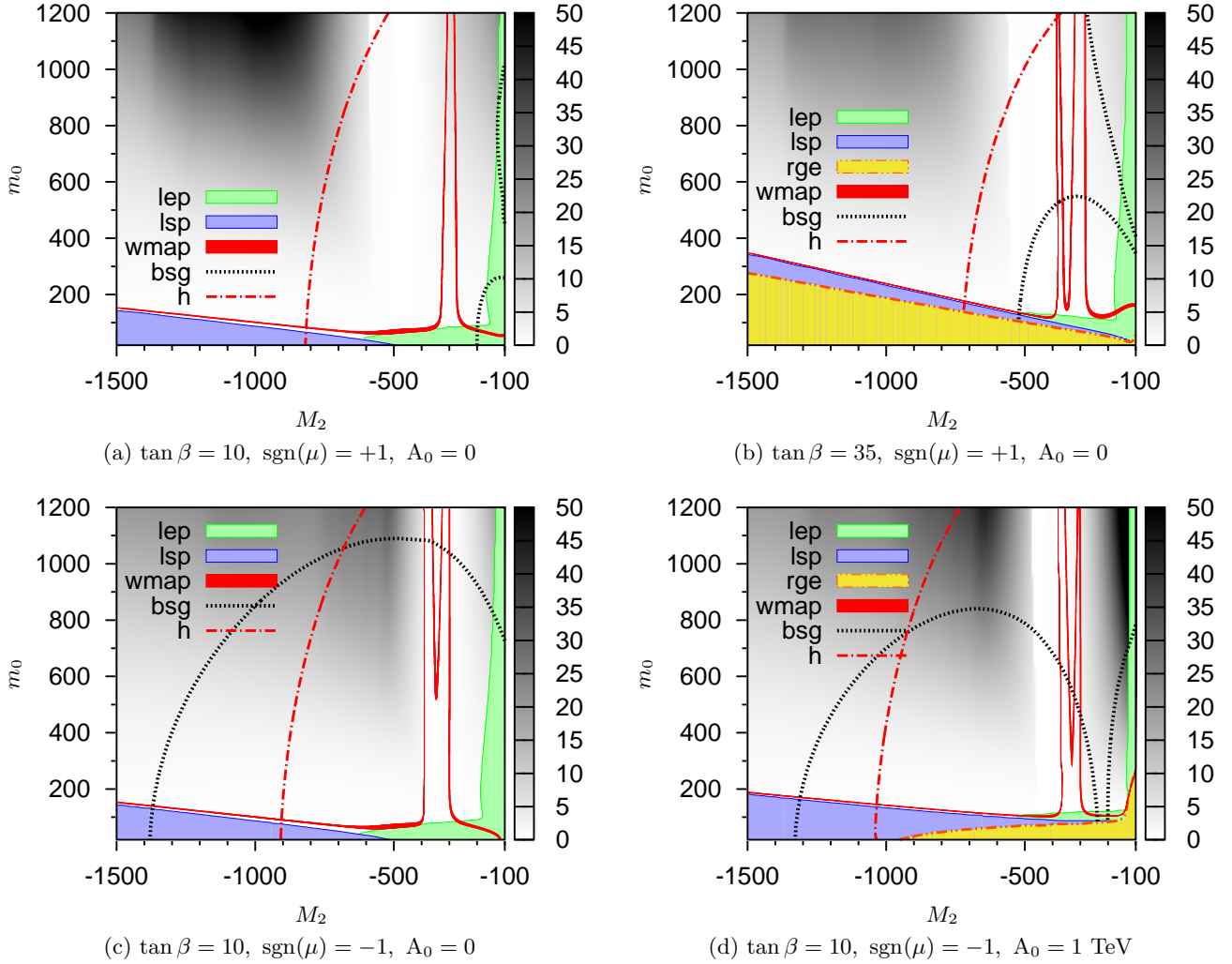


Fig. 1: Relic density  $\Omega_\chi h^2$  in the representation **24** in  $(M_2, m_0)$  plane. The dark shaded areas represent the larger relic density. **wmap** denoted filling is the WMAP preferred region, **lep** shows an area next to the axes, where the experimental mass limits are not met, **rge** shows an area where there is no radiative EWSB, and **lsp** the area where neutralino is not the LSP. **h** gives the line of  $m_h = 114$  GeV. The area between two **bsg** contours is allowed by  $b \rightarrow s\gamma$  limits in (a), (b), and (d), and above the contour in (c).

to both Z and h. The higher  $\tan\beta$  also increases the area at the low  $m_0$ , where the radiative EWSB is not possible (marked *rge*, below the area where neutralino is not the LSP).<sup>1</sup>

The same mutual sign for the  $\mu$  parameter and the gaugino mass  $M_1$  gives a slightly lower mass for the lightest neutralino than in the case with opposite sign. Since in the representation **24** the signs of  $M_1$  and  $M_2$  are the same, this effect can be seen comparing figures 1a and 1c. Thermal relic density is proportional to the mass of the particle. The  $b \rightarrow s\gamma$  constraint is also prominent in the negative  $\mu$  case [31,32,33,34,35]. We have

<sup>1</sup> It can be noted that the Higgs funnel region, which is present in singlet case, does not exist in **24** representation at large  $\tan\beta$  and large  $m_0$  values. This is due to the neutralinos, which are too light to annihilate to the heavy Higgs bosons at the resonance.

used the two sigma world average of  $BR(b \rightarrow s\gamma) = (355 \pm 24_{-10}^{+9} \pm 3) \times 10^{-6}$  for the branching fraction [36]. For example in Fig. 1c the visible area is mostly excluded by the  $2\sigma$  limit. In other figures the  $b \rightarrow s\gamma$  allowed region is between the *bsg*-denoted contours.

Switching on the trilinear scalar coupling parameter  $A_0$  increases the value of  $\mu$  through the RG evolution of the squared soft Higgs mass parameters, therefore reducing the higgsino component in the lightest neutralino. This can be seen comparing Figures 1c and 1d at the low  $|M_2|$  values. In the Fig. 1c the higgsino component of the LSP is larger at the low  $|M_2|$ -high  $m_0$  region, so the resulting relic density is lower than in Fig. 1d, where the lightest neutralino is almost purely bino.<sup>2</sup>

<sup>2</sup> In Fig. 1d the relic density can rise up to the values of 80; the shading reaches maximum saturation already in 50 in order to ease comparison with other figures.

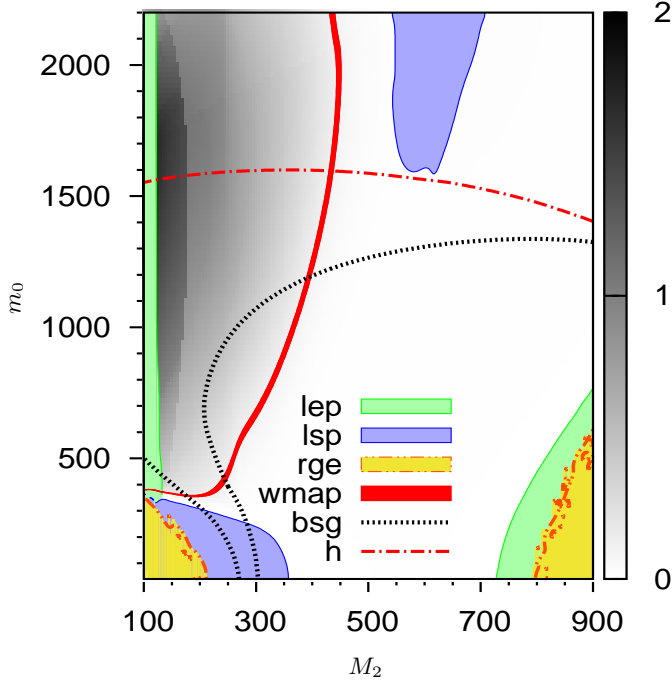


Fig. 2: Relic density  $\Omega_\chi h^2$  in the representation **75** in  $(M_2, m_0)$  plane. Explanation for the key is as in Fig. 1. The parameters used here are  $\tan\beta = 10$ ,  $\text{sgn}(\mu) = -1$ ,  $A_0 = 1$  TeV.

In Fig. 2 the contours of preferred thermal relic density in the representation **75** are plotted for one set of (GUT scale) parameters, for which appreciable region for dark matter within the WMAP limits is found, and which are not forbidden by the  $b \rightarrow s\gamma$  constraints. Since the higgsino component in the representation **75** is large [5], the resulting relic density is low, and most of the parameter space is not overclosed by the WMAP limits. Also the co-annihilations with the lightest chargino reduces the relic density, since the lightest neutralino and chargino are nearly mass degenerate in the higher  $M_2$  part of the parameter space. This is also seen in the Fig. 2 at high  $m_0$ , where the lightest chargino becomes the LSP for specific  $M_2$  values. In the low  $M_2$  region the EWSB condition pushes the  $\mu$  high, which in turn decreases the higgsino component in the lightest neutralino making it mostly a bino. The lightest neutralino and chargino are not degenerate anymore, and the relic density increases in low  $M_2$  area, which enables the emergence of the WMAP preferred region in the parameter space. The second lightest neutralino can annihilate also directly into gauge bosons in this parameter region. At the low  $m_0$  region the LSP can be the lighter stop. Again, increasing  $\tan\beta$  enhances the higgsino component leading to lower relic densities in general.

In Fig. 3 the contours of preferred thermal relic density in the representation **1** are plotted for four different sets of (GUT scale) parameters for the reference. For the chosen parameters the WMAP preferred regions are found near the  $M_2$  (i.e.  $m_{1/2}$  in mSUGRA and CMSSM language) and  $m_0$  axes.<sup>3</sup> The  $b \rightarrow s\gamma$  limits exclude large area in the figures 3c and 3d, where the sign of the  $\mu$ -parameter is negative.

In the representation **200** the higgsino mixing is large [5] and importantly, the bino-component is very small. Also the co-annihilations with the lightest chargino, which is nearly mass degenerate with the lightest neutralino, reduce the relic density substantially, and the resulting relic density is tiny. In contrast to the **75** dimensional case, the  $\mu$  parameter decreases with decreasing  $M_2$ , so the bino component does not get very large. The  $b \rightarrow s\gamma$  constraint is largely within acceptable limits (for negative  $\mu$  a bit larger  $M_2$  and  $m_0$  are required than for positive  $\mu$ ) and the LSP is mostly the lightest neutralino. Typically the Higgs mass is well above 91 GeV limit for  $\tan\beta \gtrsim 10$ , and the 114 GeV line is around  $M_2 \sim 600$  GeV. For the lower values of  $\tan\beta$ , the  $M_2$  parameter must be above 1 TeV. The parameter space suitable for finding partial neutralino dark matter can be extended both in  $m_0$  and in  $M_2$  beyond 1 TeV for both signs of  $\mu$ , but neutralino in this representation can never be the only source of dark matter.

It is possible also to have many representations simultaneously. For example, the Fig. 4 shows the relic density when two representations, **1** and **200**, are combined. If one allows the gaugino masses to be formed from two representations simultaneously, then two of the gaugino masses can be chosen freely, and only one is fixed by the representations. In Fig. 4 the parameter  $M_3$  is chosen to have a specific value ( $M_3 = 700$  GeV in Fig. 4a and  $M_3 = 400$  GeV in Fig. 4b) and  $M_2$  is allowed to vary. The overall relic density is very low, as implied by the representation **200**. However, there is a narrow peak where the relic density is enormous. This is the area, where the gaugino masses combine in such a way that the lightest neutralino is extremely light. Therefore the annihilations are very much suppressed leading to high relic density. The position of the area where this happens depends on the representations: e.g. for the representation **1**  $\oplus$  **200** the parameter  $M_1$  can be expressed as

$$M_1 = \frac{M_2(1 - 10) + M_3(10 - 2)}{1 - 2} = 9M_2 - 8M_3, \quad (7)$$

where the numbers come from the representation invariants. Therefore the minimum of the lightest neutralino mass is positioned around  $M_2/M_3 \sim 8/9$ . The  $b \rightarrow s\gamma$  constraint is within acceptable limits and the Higgs mass is above limits (in Fig. 4b  $m_h > 113.5$  GeV in otherwise

<sup>3</sup> The hyperbolic branch/focus point region [37,38], which requires a substantially larger  $m_0$ , is not found for this setup (moreover, the low scale parameterization might be more relevant in describing this region anyway [39]). Also, the  $A$ -annihilation funnel is absent, since it requires larger  $\tan\beta \sim 45 - 60$ .

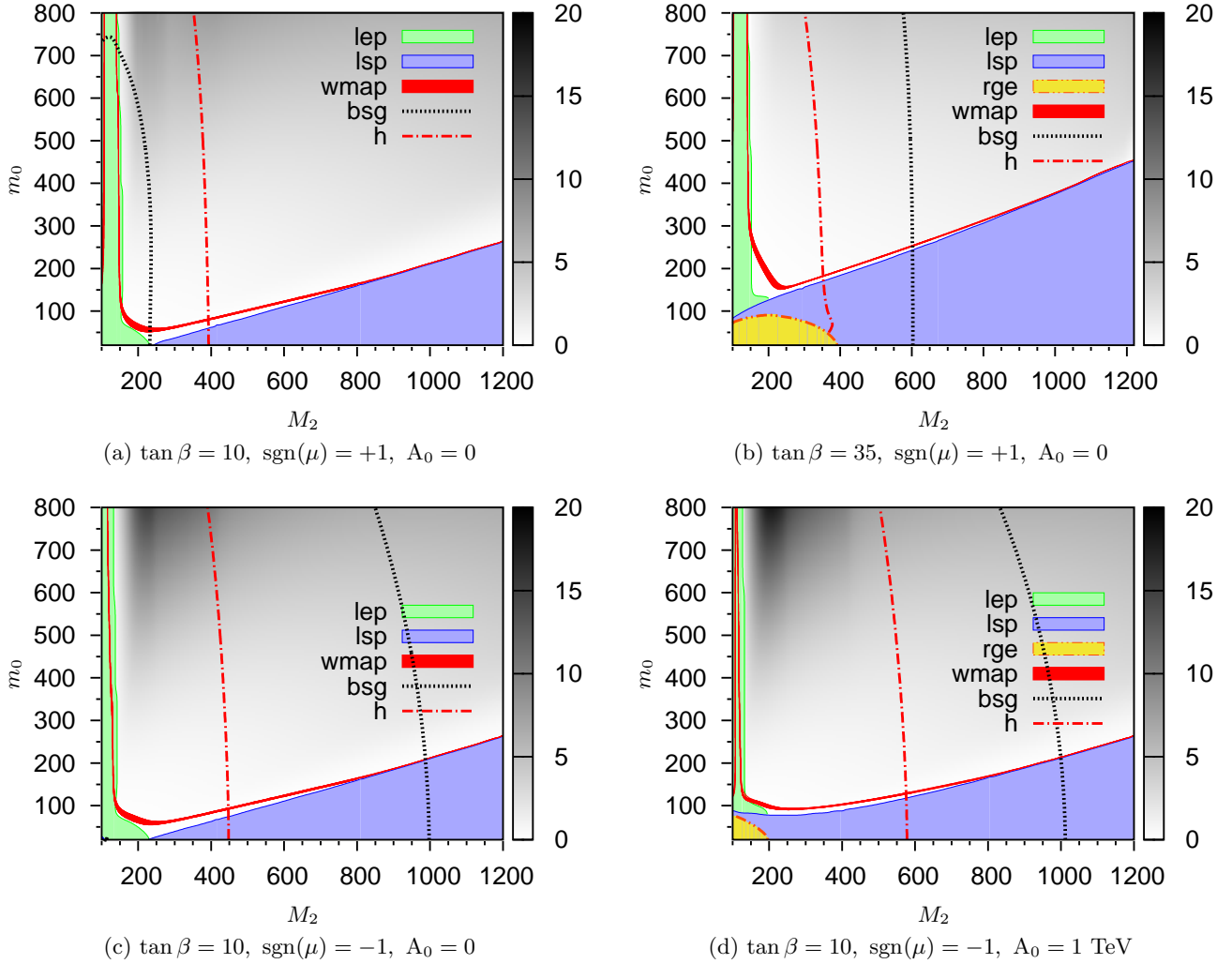


Fig. 3: Relic density  $\Omega_\chi h^2$  in the representation **1** in  $(M_2, m_0)$  plane. Explanation for the key is as in Fig. 1.

allowed regions). By increasing the value of the  $M_3$  mass parameter one effectively increases the stop masses (due to the RG evolution), which then increases the lightest Higgs mass. For example, the  $m_h > 117 \text{ GeV}$  always in the Fig. 4a. Chargino being the LSP excludes large areas in Fig. 4a. The smaller area around  $M_2 \sim 800 \text{ GeV}$  at the low  $m_0$  region is due to the stau LSP. The  $A$ -threshold is also shown as a small ring of higher relic density around  $M_2 \sim 770 \text{ GeV}$ .

Because with two representations there are two free gaugino masses, the light LSP region is always present. Therefore, if the relic density is low in general, there must also be a stripe of WMAP preferred region available. Changing the  $M_3$  mass value the WMAP preferred stripe can be moved through the parameter space, thus providing a method to fulfill the WMAP constraints.

### 3 Higgs in the neutralino cascade and dark matter

Having discussed the basic features of the SU(5) non-universal gaugino mass scenario, and the region of parameter space preferred by the thermal relic density, we describe the numerical features of the cross section of the signal events in the representation **24**. In Fig. 5 the cross section for  $\tilde{g} \rightarrow \tilde{q}q$ ,  $\tilde{q} \rightarrow \tilde{\chi}_2 q$ ,  $\tilde{\chi}_2 \rightarrow \tilde{\chi}_1 h/H/A$ ,  $h/H/A \rightarrow b\bar{b}$  produced in the pp interactions in the  $(m_A, \tan \beta)$  (figures 5a, 5c, 5e) and  $(m_A, m_{\tilde{g}})$  (figures 5b, 5d, 5f) planes are plotted. The solid (green) fill denotes the WMAP preferred relic density region. Also the Higgs 114 GeV mass contour is plotted with the contours of constant cross section (larger  $m_A$  values correspond to larger  $m_h$ ). The values of the parameters are  $(\mu = +700 \text{ GeV}/c^2$ ,  $m_{\tilde{q}} = 600 \text{ GeV}/c^2$ ,  $m_{\tilde{t}} = 350 \text{ GeV}/c^2$ , and the trilinear coupling for the top sector is chosen to be  $A_t = 800 \text{ GeV}$ ). In the  $(m_A, \tan \beta)$  figures the gluino mass is chosen as  $m_{\tilde{g}} = 770 \text{ GeV}/c^2$ , and in the  $(m_A, m_{\tilde{g}})$  plane  $\tan \beta = 10$ . In the  $(m_A, \tan \beta)$  plane the cross section



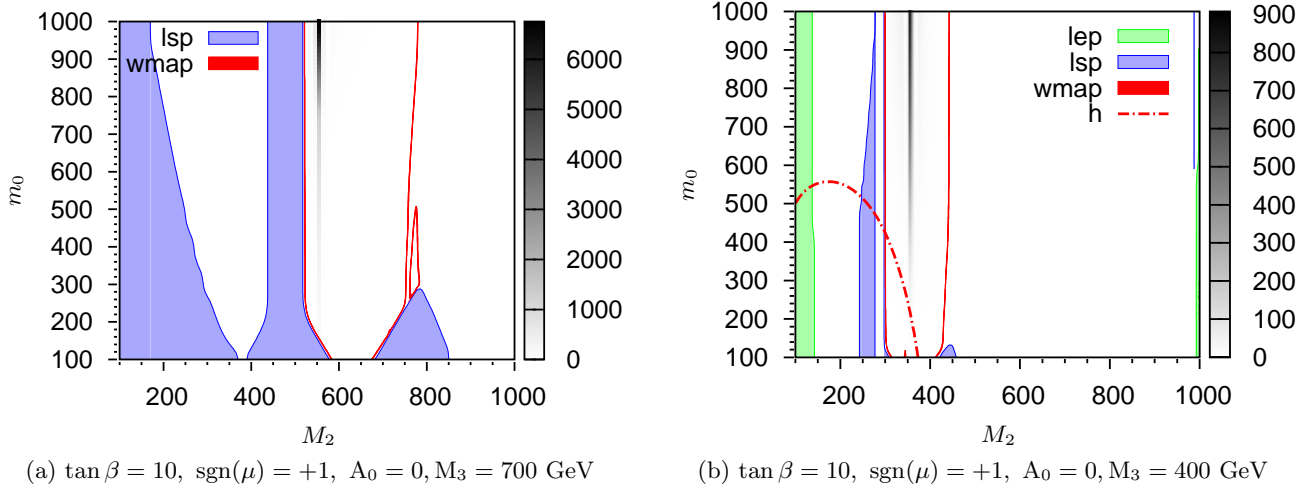


Fig. 4: Relic density  $\Omega_\chi h^2$  in the representation  $\mathbf{1} \oplus \mathbf{200}$  in  $(M_2, m_0)$  plane. Red filling is the WMAP preferred region, lep shows an area next to the axes, where the experimental mass limits are not met and lsp the area where neutralino is not the LSP. h gives the line of  $m_h = 114$  GeV.

is largest for the  $H$  Higgs production. Also the stripe of WMAP preferred relic density passes through the large cross section area. For the  $A$  production, the cross section is somewhat smaller, while for the  $h$  production it is substantially smaller for the WMAP preferred area. The near-horizontal WMAP stripe around  $\tan\beta = 8$  (beginning at  $m_A = 130$  GeV) corresponds to the closing of the Higgs resonance in the LSP annihilation: in the region below that line the lightest neutralino mass is more than half of the light Higgs boson mass, and thus the annihilation never occurs at the resonance. Heavier  $A$  correspond to the larger relic density. The relic density is lowest in between the two relic density stripes, the minimum occurring at the  $A$ -peak.

In the  $(m_A, m_{\tilde{g}})$  plane the large  $H$  production cross section is again passed by the preferred relic density stripe. The Higgs 114 GeV limit divides the parameter space in two (vertical line in the figures 5b, 5d, 5f; it should be noted, though, that for the  $\tan\beta = 10$  used here the actual Higgs boson mass limit can be as low as around 90 GeV). Also here the relic density is the lowest in between the two relic density stripes. The horizontal kink in the relic density stripe around  $m_{\tilde{g}} \sim 770$  GeV corresponds to the closing of the Higgs resonance in the LSP annihilation: in contrast to the  $(m_A, \tan\beta)$ -plots, the Higgs resonance is open below that line due to the decreasing of the lightest neutralino mass. The  $A$  and  $h$  cross sections follow the pattern of the  $(m_A, \tan\beta)$  plane, the  $A$  production cross section being slightly smaller than for  $H$  while  $h$  production is the one with the lowest cross section. The cross sections and relic densities were calculated with PROSPINO [40], SDECAY [41], HDECAY [42] and SuSpect [43] and micrOMEGAS [29, 28, 27].

Table 2 shows the mass values for  $\tilde{\chi}_1$  and  $\tilde{\chi}_2$  and the branching fractions for the  $\tilde{\chi}_2 \rightarrow h/H/A \tilde{\chi}_1$  decay channels in the representations  $\mathbf{1}$  and  $\mathbf{24}$  with  $m_A = 190$  GeV/ $c^2$  and in the representation  $\mathbf{24}$  with  $m_A = 210$  GeV/ $c^2$

with  $\tan\beta = 10$ . For the  $\mathbf{24}$ -dimensional representation all Higgs boson channels are possible. The branching fraction is largest for the CP-even neutral Higgs boson  $H$ . As the gluino mass increases, the branching fraction to  $\tilde{\chi}_2 \rightarrow h/H/A \tilde{\chi}_1$  decreases. The signal cross sections are obtained applying the  $\tilde{\chi}_2 \rightarrow h/H/A \tilde{\chi}_1$  and  $h/H/A \rightarrow b\bar{b}$  branching fractions on the total SUSY production cross section in the chosen parameter point. In the singlet case, the  $m_{\tilde{g}} = 770$  GeV is too small to allow kinematically the cascade decay. We take  $m_{\tilde{g}} = 850$  GeV, with which the decay through the light Higgs boson  $h$  is possible.

## 4 Event generation

### 4.1 SUSY cascades

The event generation and simulation were performed and the results were made public in the CMS framework [44]. The Higgs boson production in SUSY cascades was generated with PYTHIA [45] using a squark and gluino production with general MSSM simulation. The CTEQ5L structure functions [46] were used. The simulated point was  $\mu = +700$  GeV/ $c^2$ ,  $m_{\tilde{q}} = 600$  GeV/ $c^2$ ,  $m_{\tilde{t}} = 350$  GeV/ $c^2$ , and the trilinear coupling for the top sector was chosen to be  $A_t = 800$  GeV. The gluino mass was chosen as  $m_{\tilde{g}} = 770$  GeV/ $c^2$ . The U(1), SU(2) and SU(3) gaugino masses were chosen separately for each scenario, values shown in Table 3. PYTHIA version 6.325 was used within the CMKIN framework [47]. No forcing of decay channels was used. After the event generation, the events were sorted by the Higgs boson content, giving a sample of signal events, and a sample of SUSY background events with no Higgs bosons in the event. The SUSY production of multi-jet events is expected to be the main source of background.

In the Singlet representation a cross section of 18.3 pb was used for the SUSY cascade (including Higgs boson

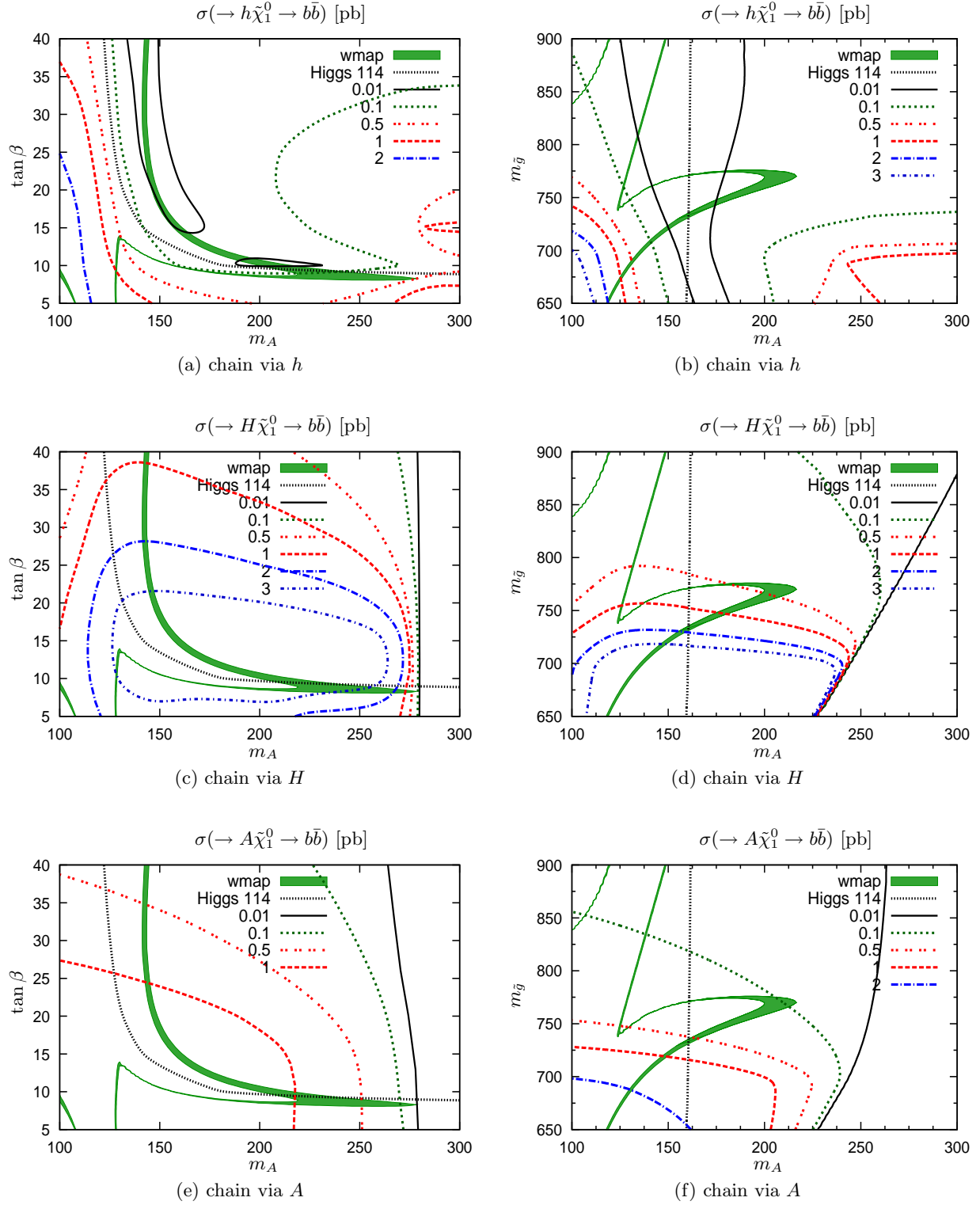


Fig. 5: Contours of constant cross section for  $pp \rightarrow h/H/A + \tilde{\chi}_1^0 + X \rightarrow b\bar{b} + \tilde{\chi}_1^0 + X$  in the  $(m_A, \tan\beta)$  (left) and  $(m_A, m_{\tilde{g}})$  (right) planes. The solid fill denotes the WMAP preferred relic density region and the dense dashed curve shows the Higgs 114 GeV mass limit (higher  $m_A$  values correspond to a higher  $m_h$ ).



Table 2: Mass values for  $\tilde{\chi}_1$  and  $\tilde{\chi}_2$  and the branching fractions for the  $\tilde{\chi}_2 \rightarrow h/H/A\tilde{\chi}_1$  decay channels in the representations **1** ( $m_{\tilde{g}} = 850$  GeV) and **24** ( $m_{\tilde{g}} = 770$  GeV) with  $m_A = 190$  GeV/ $c^2$  and in the representation **24** with  $m_A = 210$  GeV/ $c^2$  and  $\tan\beta = 10$ .

Representation, $m_A$	$m_{\tilde{\chi}_1}$ (GeV/ $c^2$ )	$m_{\tilde{\chi}_2}$ (GeV/ $c^2$ )	$\text{BR}(\tilde{\chi}_2 \rightarrow h\tilde{\chi}_1)$	$\text{BR}(\tilde{\chi}_2 \rightarrow H\tilde{\chi}_1)$	$\text{BR}(\tilde{\chi}_2 \rightarrow A\tilde{\chi}_1)$
<b>1</b> , 190 GeV/ $c^2$	120.6	246.8	0.897	0	0
<b>24</b> , 190 GeV/ $c^2$	50.5	307.4	0.00478	0.718	0.205
<b>24</b> , 210 GeV/ $c^2$	50.5	307.5	0.00144	0.739	0.161

production) with  $m_A = 190$  GeV/ $c^2$ ,  $\tan\beta = 10$ . The Higgs boson production cross section is 4.13 pb for this point. In the **24**-dimensional representation with  $m_A = 190$  GeV/ $c^2$ ,  $\tan\beta = 10$ , the cross sections are 23.1 pb and 5.07 pb, and with  $m_A = 210$  GeV/ $c^2$ ,  $\tan\beta = 10$ , 23.1 pb and 4.97 pb, respectively.

#### 4.2 Standard Model backgrounds

The  $t\bar{t}$ , QCD multi-jet, Z+jets and W+jets production are the main SM backgrounds for the Higgs boson searches with  $H/A/h \rightarrow b\bar{b}$  in SUSY cascades. The  $t\bar{t}$  events were generated with PYTHIA [45]. The production cross section was normalized to the NLO cross section of 840 pb. The QCD multi-jet background for the light Higgs boson h in the SUSY cascades has been studied with full simulation in Ref. [23] and has been found to be negligible requiring energetic jets, two b jets and large missing  $E_T$  ( $> 200$  GeV). This background particularly sensitive to the detector performance through the jet measurements. Therefore it was studied in this work with the new full simulation [48] for the  $E_T^{\text{miss}}$  cut. Events for the full simulation study were generated with PYTHIA in two bins:  $120 < p_T < 170$  GeV/c and  $170 < p_T < 230$  GeV/c. The Z+jets and W+jets events can contribute to the background through large missing  $E_T$  from  $Z \rightarrow \nu\nu$  decays and from lost leptons. These backgrounds have been investigated for the inclusive SUSY searches with ALPGEN [49] and PYTHIA simulation. The Z+jets and W+jets backgrounds have been found to be roughly on the same level as the  $t\bar{t}$  background after the basic selections for the inclusive search:  $E_T^{\text{miss}} > 200$  GeV and four jets with  $E_T > 30$  GeV [50]. The requirement of two b jets with  $E_T > 100$  GeV will suppress these backgrounds well below the  $t\bar{t}$  background and were therefore not simulated in this work.

### 5 Detector simulation

The response of the CMS detector was simulated with the fast simulation package FAMOS [51]. The pile-up corresponding to the luminosity of  $2 \times 10^{33} \text{cm}^{-2} \text{s}^{-1}$  was included. The physics objects were reconstructed with the standard methods available in the CMS reconstruction software. The primary vertex was reconstructed and selected with an algorithm searching for the highest sum of the transverse momenta of the associated tracks [52]. Jets

were reconstructed in a cone of 0.5. The b tagging was performed with a robust track counting based B-Tagging Algorithm of CMS [53]. The QCD MET reconstruction and the MET cut efficiency was studied in addition with CMS full simulation [48].

### 6 Event selection

The signal events are characterized by many energetic hadronic jets. Due to the  $m_{\tilde{g}} > m_{\tilde{q}}$  condition, the gluino decays to a quark and the corresponding squark. Therefore the cascade producing the Higgs boson contains two energetic jets from the decays of the gluino and the squark and two b jets from the decay of the Higgs boson. At least two jets are produced in the opposite cascade. The two LSP's ( $\tilde{\chi}_1^0$ ) at the end of the two cascades lead to large missing  $E_T$ . These characteristics can be used to suppress the SM backgrounds, for which the jet multiplicities and missing  $E_T$  are typically significantly smaller.

#### 6.1 Trigger

The events are supposed to be triggered with a multi-jet trigger at the Level-1 (L1) and with a combined multi-jet plus missing  $E_T$  trigger at the High Level Trigger (HLT) [54, 55]. The  $E_T$  thresholds for the four jets at the trigger level were taken to be 80, 50, 30 and 10 GeV. The threshold for the missing  $E_T$  calculated from the calorimeter cells was fixed to 135 GeV. The Level-1 trigger was not simulated. The effect of this choice is negligible since the efficiency of the multi-jet trigger on the SUSY events has been found to be close to 100% [23]. In this work the HLT efficiency in the SUSY events is found to be 67%. The  $t\bar{t}$  background is efficiently reduced already at the trigger level with the missing  $E_T$  cut. The HLT efficiency for this sample was found to be 3.8%.

#### 6.2 Jet selection

Figure 6 shows the  $E_T$  distributions for the three most energetic jets in the signal, in the SUSY background and in the  $t\bar{t}$  events. For the off-line analysis, events with four jets with  $E_T > 50$  GeV were first searched for. At this level, the  $E_T$  cuts were set to 250, 200, 100 GeV for the three most energetic jets. These cuts are more stringent than those used in Ref. [23] and thus can help to suppress

Table 3: Gaugino mass parameters for the studied points.

Representation, $m_A$	U(1)(GeV/ $c^2$ )	SU(2)(GeV/ $c^2$ )	SU(3)(GeV/ $c^2$ )
<b>1</b> , 190 GeV/ $c^2$	122.9	245.3	850
<b>24</b> , 190 GeV/ $c^2$	-44.1	-264	610
<b>24</b> , 210 GeV/ $c^2$	-45.54	-272.7	630

more efficiently the QCD multi-jet and W+jets and Z+jets backgrounds. The  $t\bar{t}$  background is reduced to 35% with the  $E_T^{\text{jet}}$  cuts. Two b jets are expected from the Higgs boson decay. Figure 7 shows the  $p_T$  distributions for the two b quarks from  $H/A \rightarrow b\bar{b}$ . Efficiency for tagging one selected jet as a b jet in the signal events, with at least one Higgs boson decaying to b quarks, was found to be about 30%. In addition to the possibility of mistagging a hadronic jet in the SUSY background, there are several sources of genuine b jets, like  $\tilde{\chi}_2 \rightarrow Z\tilde{\chi}_1$ ,  $Z \rightarrow b\bar{b}$  and gluon splitting processes in hadronic jets. As a consequence, the tagging efficiency in the SUSY background was found to be substantial, about 13%.

Figure 8 shows the distribution of the missing  $E_T$  for the signal, for the SUSY background and for the  $t\bar{t}$  events. Large missing  $E_T$  is typical for SUSY events due to the presence of neutralinos in the final state. The  $t\bar{t}$  background is further suppressed with this cut by a factor of  $\sim 5$ . The QCD multi-jet production contributes to the background through missing  $E_T$  due to detector resolution and mis-measurement of jets. The missing  $E_T$  selection was studied with the new full simulation package [48]. Efficiency for  $E_T^{\text{miss}} > 200$  GeV was found to be  $4 \times 10^{-5}$  for  $120 < p_T < 170$  GeV/c and  $9 \times 10^{-5}$  for  $170 < p_T < 230$  GeV/c. No trigger simulation was included in the estimation of this background.

Due to the large jet multiplicity and the mistagging possibility, the combinatorial background from false jet assignment can be expected to be large for the reconstruction of the Higgs boson invariant mass from the b jets. This combinatorial background can be significantly reduced with a method called a hemisphere separation technique, devised in [56]. This method separates the jets into two “hemispheres” where the initial gluino or squark jet originates, starting from the most energetic jet in the two hemispheres. The assignment of a jet to the axis is performed exploiting the angles and invariant masses. The method has been shown to be effective in removing the combinatorial background arising from jet multiplicity in SUSY events in Ref. [23].

After the separation to hemispheres the b jets were selected in each hemisphere separately. Due to the large mass of the decaying neutralino, the Higgs boson, in particular the light Higgs boson h, receives a large boost leading to a small separation angle between the b jets. The  $\Delta R$  ( $\Delta R = \sqrt{(\Delta\eta)^2 + (\Delta\phi)^2}$ ) between the two b quarks from the Higgs boson, shown in Fig. 9 for the light Higgs boson, is peaked around  $\Delta R \sim 1$ . Therefore the pair of b jets with the lowest  $\Delta R$  value was selected in each hemisphere. Among these two combinations the one with lower  $\Delta R$  value was taken to present the Higgs boson.

Figure 10 shows the  $b\bar{b}$  mass distribution for the signal in the singlet representation with  $m_A = 190$  GeV/ $c^2$ . Only the light Higgs boson can be produced due to the small mass difference between the two neutralinos. The mass distribution with correct b-jet mass assignments is also shown in the figure. The tagged b jet is defined as a genuine b jet if a b quark is found within  $\Delta R < 0.4$  from the jet axis. The fraction of correct jet assignments is 29%. Large fraction of the false b-jet assignments is distributed to large mass values. A tail at large masses is visible also in the mass distribution with correct assignments. This tail is due to overlapping jets in the multi-jet environment. Figure 11 shows the  $b\bar{b}$  mass distribution for the signal in the representation **24** with  $m_A = 190$  GeV/ $c^2$ . For this parameter point the mass difference between the neutralinos is large and the decay branching fractions to heavy Higgs bosons are significant. The fraction of the light Higgs boson after all selection cuts is 3.5%. For the heavy Higgs bosons, better signal mass resolution and signal visibility was obtained with a significantly harder cut for the selected b jets,  $E_T > 100$  GeV, as is shown in the Fig. 11. About 87% of the signal is due to the heavy CP-even Higgs boson H. The mass distribution with correct b-jet mass assignments and with  $E_T > 100$  GeV is also shown in the figure. The opening angle in the Higgs boson decay is larger than for the light Higgs boson h in the singlet representation making more favorable the jet reconstruction and b-jet identification. The fraction of correct jet assignments was found to be 39%.

### 6.3 Signal over background ratios

Figure 12 shows the  $b\bar{b}$  mass distribution for the signal in the singlet representation with  $m_A = 190$  GeV/ $c^2$  and  $\tan\beta = 10$  and for the total background. The  $t\bar{t}$  background is shown separately in the figure. Setting an upper bound of  $\Delta R < 1.5$  could reduce this tail as can be seen from Fig. 13. To further reduce the backgrounds correlations between the reconstructed  $b\bar{b}$  pair, presenting the Higgs boson, and the missing  $E_T$  was studied. The missing  $E_T$  originates from the  $\tilde{\chi}_2$  decays at the end of the two cascades. Therefore, the missing  $E_T$  can be expected to follow one of the hemisphere axis. It was found to follow preferentially the selected  $b\bar{b}$  pair, as can be seen from Fig. 14 showing the  $\Delta\phi$  distribution between the  $b\bar{b}$  system and the missing  $E_T$ . Figure 15 shows the invariant mass distribution with  $\Delta\phi(\text{Higgs}, E_T^{\text{miss}}) < 120^\circ$ .

Figures 16 and 17 show the invariant mass distributions for the signal and background in the **24**-dimensional representation with  $m_A = 190$  and 210 GeV/ $c^2$  and with  $E_T^{\text{bjet}} > 100$  GeV.

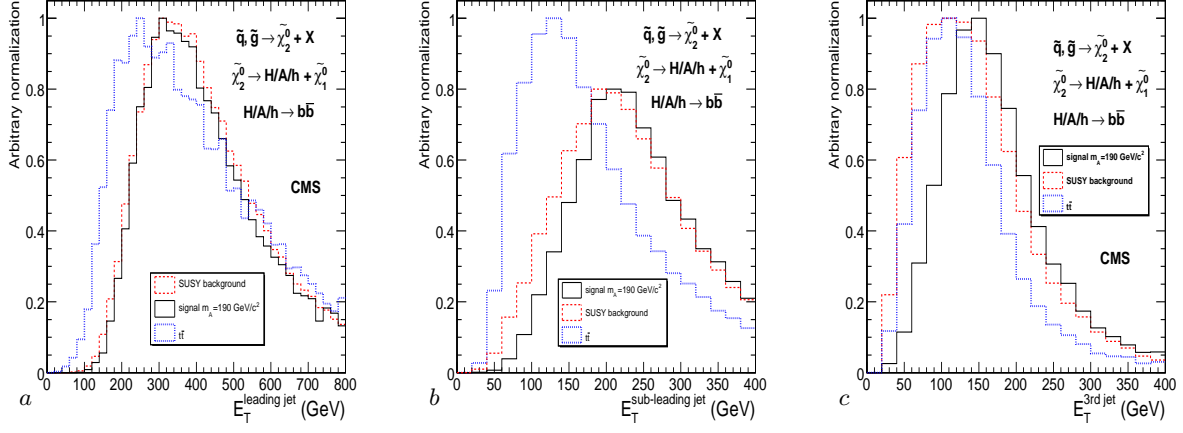


Fig. 6: Distribution of  $E_T$  of the most energetic jet (a), the sub-leading jet (b), and the third most energetic jet (c) for the signal with  $m_A = 190 \text{ GeV}/c^2$  and  $\tan\beta = 10$  (solid line), for the SUSY background (dashed line) and for the  $t\bar{t}$  background (dotted line) in the representation **24**.

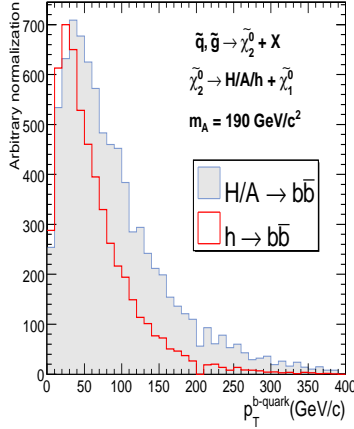


Fig. 7: Distribution of  $p_T$  for the b quarks from  $H/A \rightarrow b\bar{b}$  (filled histogram) and from  $h \rightarrow b\bar{b}$  (solid line) for the signal with  $m_A = 190 \text{ GeV}/c^2$  in the representation **24**.

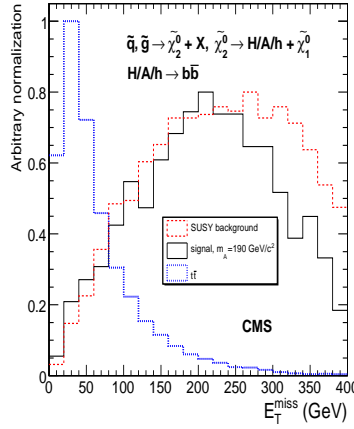


Fig. 8: Distribution of missing  $E_T$  for the signal with  $m_A = 190 \text{ GeV}/c^2$  and  $\tan\beta = 10$  (solid line) in the representation **24**, for the SUSY background (dashed line) and for the  $t\bar{t}$  background (dotted line).

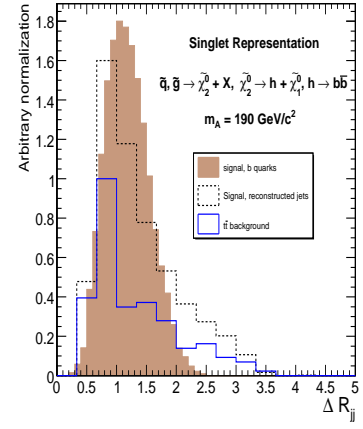


Fig. 9: Distribution of  $\Delta R$  between the selected jets for the signal in the singlet representation with  $m_A = 190 \text{ GeV}/c^2$ , and for the  $t\bar{t}$  background. The  $\Delta R$  between the b quarks from the Higgs boson decay also shown.

The selection cuts are summarized below:

- At least 4 reconstructed jets with  $E_T > 50 \text{ GeV}$
- One jet with  $E_T > 200 \text{ GeV}$
- Two jets with  $E_T > 150 \text{ GeV}$
- Three jets with  $E_T > 100 \text{ GeV}$
- At least 2 b jets with  $E_T > 50 \text{ GeV}$  for the light Higgs boson h and at least 2 b jets with  $E_T > 100 \text{ GeV}$  for the heavy Higgs bosons
- Missing  $E_T$  over  $200 \text{ GeV}$

The number of events after each cut and relative cut efficiencies are shown in Tables 4 and 5. The QCD background was estimated without trigger simulation and with

full simulation for the efficiency of the  $E_T^{\text{miss}} > 200 \text{ GeV}$  cut.

## 7 Estimation of statistical significance

The event selection procedure described above yields a visible signal in the  $b\bar{b}$  mass as can be seen from Figs. 12 - 17. Therefore the background shape can be determined with fits to the side-bands of the peak. Approximately 50% of the background level in the signal area is due to the combinatorial background. For the light and heavy Higgs bosons

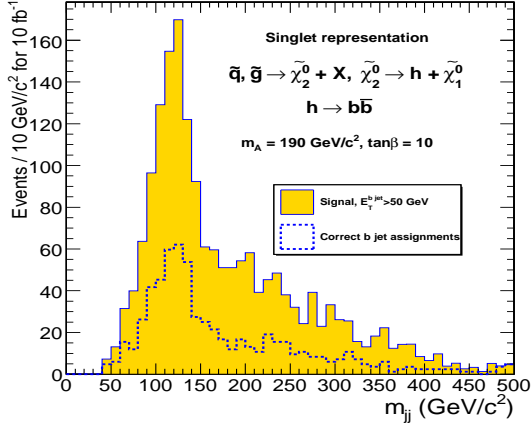


Fig. 10: Invariant mass of the two b jets (filled histogram) in the singlet representation. The mass distribution with correct b jet assignments is shown with dashed line.

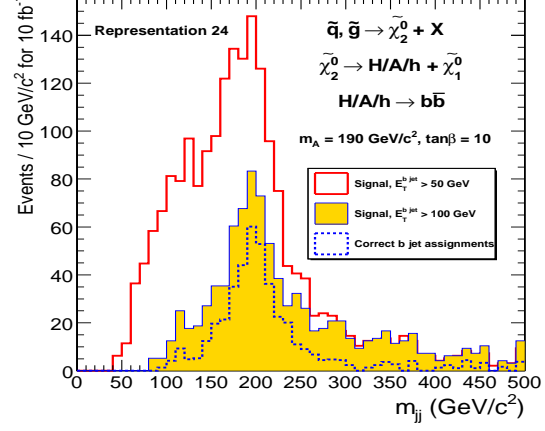


Fig. 11: As in Fig. 10, for **24** representation with two different  $E_T^{\text{bjet}}$  cuts. The mass distribution with correct b jet assignments is shown for  $E_T^{\text{bjet}} > 100$  GeV.

Table 4: Cross section times branching fraction, number of events for  $10 \text{ fb}^{-1}$  and percentage cut efficiencies (in brackets) for the H/A signal with  $m_A = 190 \text{ GeV}/c^2$  and for the SUSY background in the **24** dimensional representation with  $\tan\beta = 10$ . The results for the  $t\bar{t}$  and QCD backgrounds are also shown. For the QCD background the efficiency for  $E_T^{\text{Miss}} > 200 \text{ GeV}$  was calculated with full simulation [48], without trigger simulation.

rep 24	Signal		SUSY		t $\bar{t}$	QCD
$\sigma \times \text{BR}$ (pb)	5.07		18.05		840	$6.29 \times 10^4$
L1+HLT	36118	(71.2)	$1.51 \times 10^5$	(83.7)	$3.16 \times 10^5$	(3.8)
At least 4 jets, $E_T > 50 \text{ GeV}$	23232	(64.3)	$1.28 \times 10^5$	(84.6)	$2.54 \times 10^5$	(80.4)
$E_T^{\text{Miss}} > 200 \text{ GeV}$	22871	(98.5)	96382	(75.4)	48831	(19.2)
$E_T^{\text{jet}}$ cuts	17315	(75.7)	53558	(55.6)	17352	(35.5)
At least 2 b jets, $E_T > 100 \text{ GeV}$	4663	(26.9)	4335	(8.1)	3528	(20.3)
Jet pairing selection	948	(20.3)	503	(11.6)	292	(8.3)

Table 5: Cross section times branching fraction, number of events for  $10 \text{ fb}^{-1}$  and prosentual cut efficiencies (in brackets) for the h signal with  $m_A = 190 \text{ GeV}/c^2$  and for the SUSY background in the singlet representation with  $\tan\beta = 10$ . The results for the  $t\bar{t}$  are also shown.

rep 1	Signal		SUSY		t $\bar{t}$	
$\sigma \times \text{BR}$ (pb)	4.13		14.2		840	
L1+HLT	31782	(64.8)	119582	(50.4)	$3.16 \times 10^5$	(3.8)
At least 4 jets, $E_T > 50 \text{ GeV}$	30682	(96.9)	96548	(80.7)	$2.54 \times 10^5$	(80.4)
$E_T^{\text{Miss}} > 200 \text{ GeV}$	20627	(67.2)	73157	(75.8)	48831	(19.2)
$E_T^{\text{jet}}$ cuts	15315	(74.2)	48260	(66.0)	17352	(35.5)
At least 2 b jets, $E_T > 50 \text{ GeV}$	5494	(35.9)	5570	(11.5)	5098	(29.4)
Jet pairing selection	1813	(33.0)	839	(15.1)	606	(11.9)
$\Delta\phi(\text{Higgs}, E_T^{\text{miss}}) < 120^\circ$	866	(69.5)	254	(51.6)	235	(61.8)

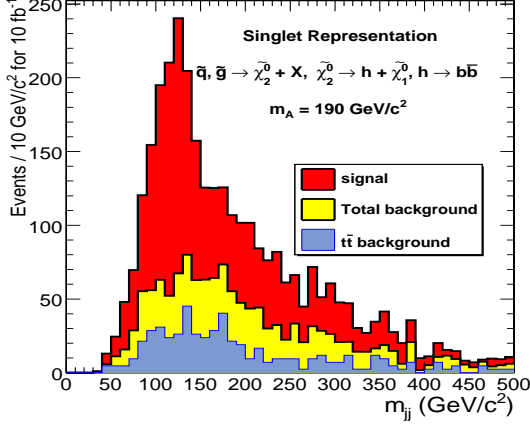


Fig. 12: Distribution of the invariant mass reconstructed from the selected b jets for the signal, for the total background and for the  $t\bar{t}$  background in the singlet representation with  $m_A = 190 \text{ GeV}/c^2$ .

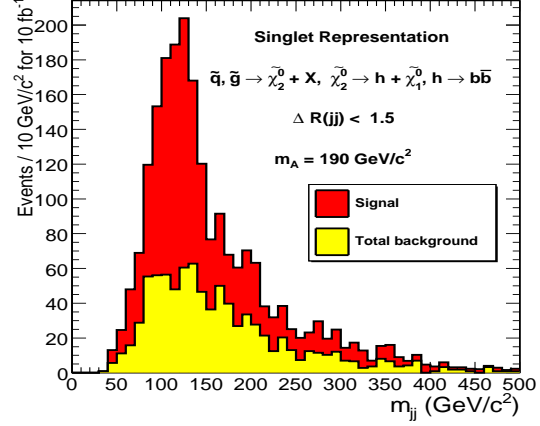


Fig. 13: Distribution of the invariant mass reconstructed from the selected b jets for the signal, for the total background with  $\Delta R(jj) < 1.5$  in the singlet representation with  $m_A = 190 \text{ GeV}/c^2$ .

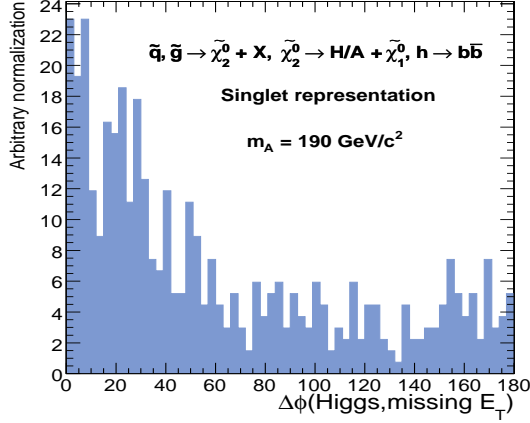


Fig. 14: Distribution of  $\Delta\phi$  between the Higgs boson reconstructed from the selected b jets and missing  $E_T$  for reconstructed missing  $E_T$  (solid histogram) and for missing  $E_T$  reconstructed at the generator level (solid line) in the singlet representation with  $m_A = 190 \text{ GeV}/c^2$ .

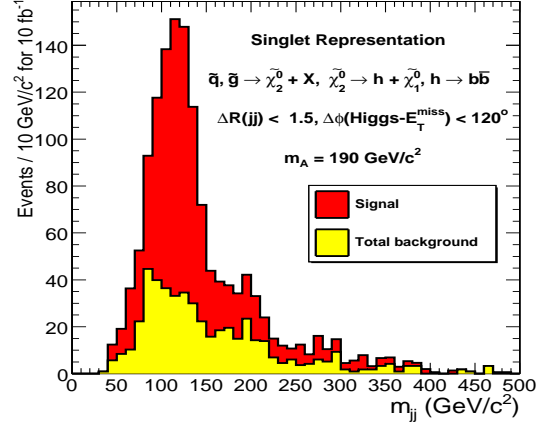


Fig. 15: Distribution of the invariant mass reconstructed from the selected b jets for the signal, for the total background with  $\Delta R(jj) < 1.5$  and  $\Delta\phi(\text{Higgs}, E_T^{\text{miss}}) < 120^\circ$  in the singlet representation with  $m_A = 190 \text{ GeV}/c^2$ .

with  $m_A = 190 \text{ GeV}/c^2$  in the **24**- and **1**-dimensional representations the background areas were taken as those outside the intervals of  $120 < m_{b\bar{b}} < 250 \text{ GeV}/c^2$  and  $80 < m_{b\bar{b}} < 150 \text{ GeV}/c^2$ , respectively. An interval of  $150 < m_{b\bar{b}} < 250 \text{ GeV}/c^2$  was used for  $m_A = 210 \text{ GeV}/c^2$  in the **24**-dimensional representation. The background distributions were obtained fitting a  $5^{th}$ -order polynomial to the sidebands of the mass peaks, the areas outside the mass windows given above. The full mass distributions were then fitted combining the obtained polynomial and a Gaussian distribution. The expected number of background events was extracted from extrapolations of the background fits to the signal area. The signal events are then given as the difference between the measured number of events and the expected number of background events

from the fit. Table 6 shows the mass intervals, the fitted Higgs boson mass values and the resulting statistical significance. Figures 18 - 20 show the fitted mass distributions for the signal and backgrounds.

To estimate the statistical significance a likelihood-ratio method was used starting from the shapes of the fitted distributions for the signal+background and for background alone. A new “toy experiment” was formed fluctuating each bin in the distribution according to a Poisson distribution with the smeared bin value as a mean. The new distribution was refitted with the signal (Gaussian) and background (5th order polynomial) shapes. This procedure was repeated many (1000) times. For each experiment, a statistical significance was calculated according

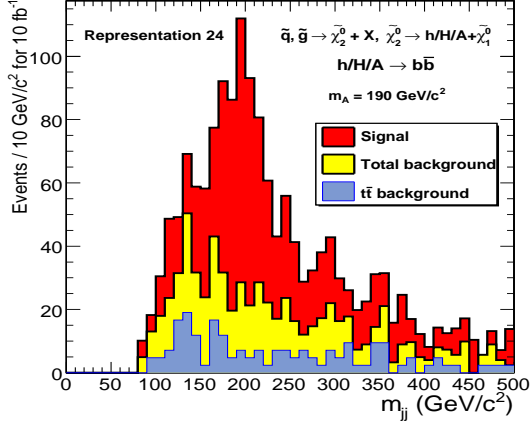


Fig. 16: Distribution of the invariant mass reconstructed from the selected b jets for the signal, for the total background and for the  $t\bar{t}$  background in the representation **24** for  $m_A = 190 \text{ GeV}/c^2$  with  $E_T > 100 \text{ GeV}$  for the tagged b jets.

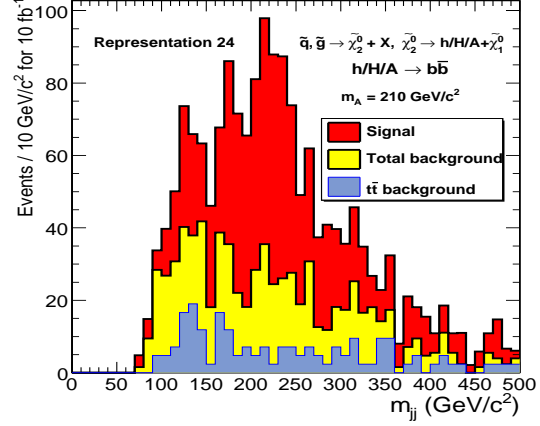


Fig. 17: Distribution of the invariant mass reconstructed from the selected b jets for the signal, for the total background and for the  $t\bar{t}$  background in the representation **24** for  $m_A = 210 \text{ GeV}/c^2$  with  $E_T > 100 \text{ GeV}$  for the tagged b jets.

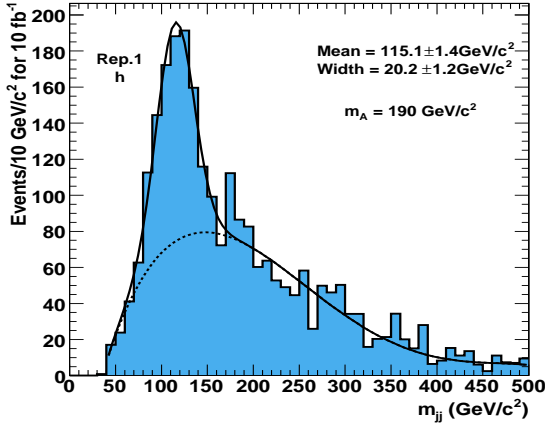


Fig. 18: Fit of a Gaussian plus a 5th degree polynomial to the  $b\bar{b}$  invariant mass for the signal and the total background in the singlet representation with  $m_A = 190 \text{ GeV}/c^2$ .

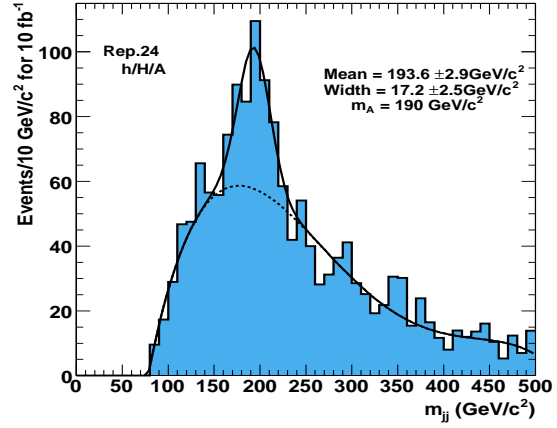


Fig. 19: Fit of a Gaussian plus a 5th degree polynomial to the  $b\bar{b}$  invariant mass for the signal and the total background in the **24**-representation with  $m_A = 190 \text{ GeV}/c^2$ .

Table 6: Higgs boson mass window used for the fits, Higgs boson mass and statistical significance obtained from fits with likelihood-ratio method starting from the shapes of the fitted distributions.

	rep24, $m_A = 190 \text{ GeV}/c^2$	rep24, $m_A = 210 \text{ GeV}/c^2$	rep1, $m_A = 190 \text{ GeV}/c^2$
$\Delta m \text{ (GeV}/c^2\text{)}$	150 - 250	150 - 250	70 - 150
$m_{\text{Higgs}} \text{ (GeV}/c^2\text{)}$	$193.6 \pm 2.9$	$224.7 \pm 3.7$	$118.5 \pm 1.5$
Significance	9.5	5.6	21.2



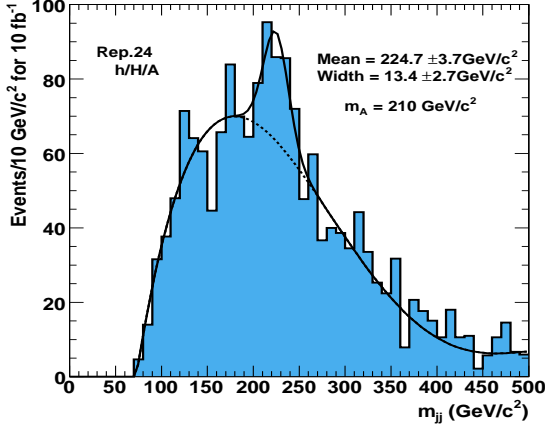


Fig. 20: Fit of a Gaussian plus a 5th degree polynomial to the  $b\bar{b}$  invariant mass for the signal and the total background in the **24**-representation with  $m_A = 210 \text{ GeV}/c^2$ .

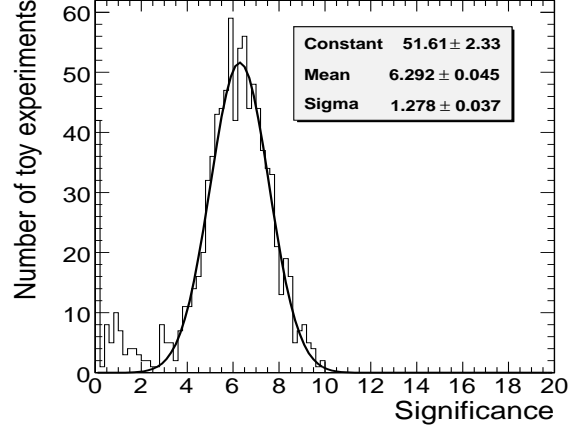


Fig. 21: Distribution of the likelihood-ratio estimator  $\sigma_L$  for  $\tilde{q}, \tilde{g} \rightarrow \tilde{\chi}_1 H/A \rightarrow \tilde{\chi}_1 b\bar{b}$  in the representation **24** for  $m_A = 210 \text{ GeV}/c^2$ .

to the following likelihood-ratio estimator:

$$\sigma_L = \sqrt{2 \ln(L_{S+B}/L_B)} \quad (8)$$

where  $L_{S+B}$  is the maximum likelihood value obtained in the signal+background binned likelihood fit, and  $L_B$  is the maximum likelihood value from the binned background-only hypothesis fit. Figure 21 shows the distribution of  $\sigma_L$  for  $m_A = 190 \text{ GeV}/c^2$  in the **24**-dimensional representation with  $10 \text{ fb}^{-1}$ . The distribution has a Gaussian shape with width close to unity. The statistical significance can be therefore obtained as a mean value of a Gaussian fit and is 8.6 for  $m_A = 190 \text{ GeV}/c^2$ . The same procedure was performed for  $m_A = 210 \text{ GeV}/c^2$ . The fitting procedure was found to be quite robust and not sensitive to the chosen signal region. No systematic uncertainties are included. The background shape and the form of the function to fit it was assumed to be determined from MC studies. The SM backgrounds will be ultimately measured from the data.

## 8 Methods to measure the backgrounds from data

Methods to measure the SM backgrounds from data have been developed in CMS [50]. Missing  $E_T$  in the QCD multi-jet events is mainly due to detector resolution and mis-measured jets. Contribution from badly measured jets can be suppressed with topological cuts, excluding events where the missing  $E_T$  is parallel to the leading jet. For the QCD background, cleaned as much as possible from the mis-measured jets, the shape and normalization could be obtained measuring the multi-jet events with low  $E_T$  thresholds, where the SUSY contribution is insignificant, and extrapolating the  $E_T^{\text{Miss}}$  distribution to the area of the SUSY searches. Due to large cross section of the QCD

multi-jet background the contamination from  $t\bar{t}$  events is small and could be suppressed demanding that no b-jets are present in the sample.

The large  $E_T^{\text{Miss}}$  values in the  $t\bar{t}$  events with hadronic selection are due to detector resolution, mis-measured jets, un-identified leptons from W decays, semileptonic decays of b and c quarks and hadronic  $\tau$  decays from  $W \rightarrow \tau\nu$ . As for the QCD multi-jet background the contribution from mis-measured jets can be suppressed with topological cuts. The hadronic  $\tau$  decays and the leptons in jets can be efficiently identified with the newly developed Particle Flow methods [57]. Requirement of two well identified b jets and a well measured hadronic top mass may not be, however, enough to suppress a contamination from QCD multi-jet background for the selection of  $t\bar{t}$  events with low  $E_T$  thresholds. Therefore, the hadronic  $t\bar{t}$  background may have to be estimated with Monte-Carlo methods.

## 9 Discovery potential

Figure 22 shows the  $5\sigma$ -discovery potential for Higgs boson production in the SUSY cascades  $\tilde{g} \rightarrow \tilde{q}q$ ,  $\tilde{q} \rightarrow \tilde{\chi}_2 q$ ,  $\tilde{\chi}_2 \rightarrow \tilde{\chi}_1 h/H/A$ ,  $h/H/A \rightarrow b\bar{b}$  in the non-universal **24** dimensional representation for integrated luminosity of  $10 \text{ fb}^{-1}$ . Two mass points,  $m_A = 190$  and  $210 \text{ GeV}/c^2$  were investigated. The discovery potential was scanned by renormalizing the signal and SUSY background cross sections as a function of  $\tan\beta$ . The cross sections were calculated as described in Section 3. Constant signal and background selection efficiency as a function of  $\tan\beta$  was assumed.

The discovery region extends to masses of  $\sim 210 \text{ GeV}/c^2$  around  $\tan\beta = 10$  and to  $\sim 190 \text{ GeV}/c^2$  around  $\tan\beta = 30$ . For  $\sim 190 \text{ GeV}/c^2$  the low  $\tan\beta$  region was covered with better than  $5\sigma$  significance down to  $\tan\beta = 2$  which was the lowest value of  $\tan\beta$  studied. Since the cross section for

$H/A$  production decreases rapidly at Higgs masses around  $\sim 280 \text{ GeV}/c^2$ , the discovery region is not expected to cover the high Higgs mass values of  $(m_A, \tan\beta)$  parameter space even with high luminosities. However, large fraction of the WMAP preferred relic density region can be explored with this channel at the LHC already with  $10 \text{ fb}^{-1}$ .

The systematic uncertainties are not included in the result of Fig. 22. The main source of systematic uncertainties is due to the uncertainty of the jet energy scale,  $\sim 10\%$  [50], which can affect the efficiency of selecting the 4 jets and the efficiency of the  $E_T^{\text{Miss}}$  cut. Further sources of systematic uncertainty are the b-tagging ( $\sim 5\%$ ) and the luminosity measurements ( $\sim 5\%$ ) [50]. The theoretical uncertainty on the  $t\bar{t}$  cross section due to variation of the scale and PDF is about 6% [50]. The MC statistics of the  $t\bar{t}$  background used in this work corresponds to  $2.4 \text{ fb}^{-1}$ , which causes an additional uncertainty of about 4% on the level of this background after selection. Including the systematic uncertainties of similar level has been shown in Ref. [50] to degrade the discovery limits in the SUSY parameter space only slightly for integrated luminosities up to  $10 \text{ fb}^{-1}$ . In particular, the reach for the jet+MET channel has been shown to vary by  $\lesssim 5\%$  as a function of  $m_0$  and  $m_{1/2}$  for  $10 \text{ fb}^{-1}$ . Similar variation ( $\sim 10 \text{ GeV}/c^2$ ) can be expected for the reach of Fig. 22 in  $m_A$ .

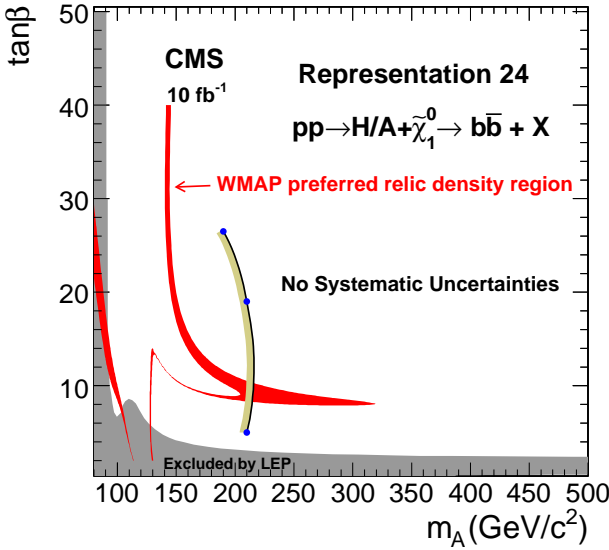


Fig. 22: CMS discovery potential at  $5\sigma$  level for  $\tilde{q}, \tilde{g} \rightarrow \tilde{\chi}_1 H/A \rightarrow \tilde{\chi}_1 b\bar{b}$  in the representation **24** with an integrated luminosity of  $10 \text{ fb}^{-1}$ . No systematic uncertainties are included.

## 10 Conclusions

The dark matter allowed regions in the  $SU(5)$  GUT representations were studied. From these representations all but the singlet lead to non-universal gaugino masses. It

was demonstrated that combinations of different representations can give observed dark matter for otherwise experimentally allowed parameter values. In the representation **24** the Higgs signal from the neutralino decay is interesting and different from the usual universal singlet model. Therefore this work especially concentrated on this representation. The preferred dark matter regions for several parameter selections were showed and analyzed, including the points studied with realistic detector simulations.

To study the discovery potential at the LHC, the Higgs boson, produced in one of the SUSY cascades, was assumed to decay to b quarks. Event selection was based on the requirement of large missing  $E_T$ , four energetic jets of which two tagged b jets. The combinatorial background from false jet assignments was reduced by separating the jets into two hemispheres. Contributions from the SUSY and SM ( $t\bar{t}$ ) backgrounds were found to be comparable. Visible signals were obtained as a function of the  $b\bar{b}$  invariant mass. A likelihood-ratio method was used to extract the statistical significance. The simulation work showed that a  $5\sigma$ -discovery can be expected up to the masses of  $m_A = 190 - 210 \text{ GeV}/c^2$  for  $\tan\beta = 5-35$ . The WMAP preferred relic density region, excluding those for  $\tan\beta \sim 8-10$ , can be explored at the LHC in the representation **24** with the  $\tilde{g} \rightarrow \tilde{q}q$ ,  $\tilde{q} \rightarrow \tilde{\chi}_2 q$ ,  $\tilde{\chi}_2 \rightarrow \tilde{\chi}_1 h/H/A$ ,  $h/H/A \rightarrow b\bar{b}$  cascades in SUSY events with the integrated luminosity of  $10 \text{ fb}^{-1}$ .

## Acknowledgments

The authors would like to thank U. Berzano, F. Moortgat and A. Nikitenko for helpful discussions. SR acknowledges the kind hospitality of the Helsinki Institute of Physics during the final stages of this work. Financial support from the Academy of Finland (Project number 115032) is acknowledged. The work of JL is supported in part by Bundesministerium für Bildung und Forschung, Berlin-Bonn.

## References

1. E. Cremmer, S. Ferrara, L. Girardello, and Antoine Van Proeyen. Coupling supersymmetric yang-mills theories to supergravity. *Phys. Lett.*, B116:231, 1982.
2. John R. Ellis, K. Enqvist, Dimitri V. Nanopoulos, and K. Tamvakis. Gaugino masses and grand unification. *Phys. Lett.*, B155:381, 1985.
3. Manual Drees. Phenomenological consequences of  $N = 1$  supergravity theories with nonminimal kinetic energy terms for vector superfields. *Phys. Lett.*, B158:409, 1985.
4. G. Anderson, C.H. Chen, J.F. Gunion, J.D. Lykken, T. Moroi, and Y. Yamada. Motivations for and implications of non-universal GUT-scale boundary conditions for soft SUSY-breaking parameters. 1996. hep-ph/9609457.
5. Katri Huitu, Jari Laamanen, Pran N. Pandita, and Sourov Roy. Phenomenology of non-universal gaugino masses in supersymmetric grand unified theories. *Phys. Rev.*, D72:055013, 2005.

6. Greg Anderson, Howard Baer, Chih-hao Chen, and Xerxes Tata. The reach of fermilab tevatron upgrades for SU(5) supergravity models with nonuniversal gaugino masses. *Phys. Rev.*, D61:095005, 2000.
7. Katri Huitu, Yoshiharu Kawamura, Tatsuo Kobayashi, and Kai Puolamaki. Phenomenological constraints on SUSY SU(5) GUTs with nonuniversal gaugino masses. *Phys. Rev.*, D61:035001, 2000.
8. G Belanger, F Boudjema, A Cottrant, A Pukhov, and A Semenov. WMAP constraints on SUGRA models with non-universal gaugino masses and prospects for direct detection. *Nucl. Phys.*, B706:411, 2005.
9. A Djouadi, Y Mambrini, and M Muhlleitner. Chargino and neutralino decays revisited. *Eur. Phys. J.*, C20:563, 2001.
10. Utpal Chattopadhyay, Debajyoti Choudhury, and Debotam Das. Large evolution of the bilinear Higgs coupling in supersymmetric models and reduction of phase sensitivity. *Phys. Rev.*, D72:095015, 2005.
11. Utpal Chattopadhyay and Pran Nath.  $b - \tau$  unification,  $g(\mu) - 2$ , the  $b \rightarrow s + \gamma$  constraint and nonuniversalities. *Phys. Rev.*, D65:075009, 2002.
12. Subhaditya Bhattacharya, Aresh Krishna Datta, and Biswarup Mukhopadhyaya. Non-universal gaugino masses: a signal-based analysis for the Large Hadron Collider. *JHEP*, 10:080, 2007.
13. Achille Corsetti and Pran Nath. Gaugino mass nonuniversality and dark matter in SUGRA, strings and D-brane models. *Phys. Rev.*, D64:125010, 2001.
14. Vincent Bertin, Nezri Emmanuel, and Jean Orloff. Neutralino dark matter beyond CMSSM universality. *JHEP*, 02:046, 2003.
15. Andreas Birkedal-Hansen and Brent D. Nelson. Relic neutralino densities and detection rates with nonuniversal gaugino masses. *Phys. Rev.*, D67:095006, 2003.
16. Utpal Chattopadhyay and D P. Roy. Higgsino dark matter in a SUGRA model with nonuniversal gaugino masses. *Phys. Rev.*, D68:033010, 2003.
17. Utpal Chattopadhyay, Achille Corsetti, and Pran Nath. Supersymmetric dark matter and yukawa unification. *Phys. Rev.*, D66:035003, 2002.
18. D. G. Cerdeno and C. Munoz. Neutralino dark matter in supergravity theories with non- universal scalar and gaugino masses. *JHEP*, 10:015, 2004.
19. S. F. King, J. P. Roberts, and D. P. Roy. Natural dark matter in SUSY GUTs with non-universal gaugino masses. 2007.
20. H. Baer, M. Bisset, X. Tata, and J. Woodside. *Phys. Rev.*, D46:303, 1992.
21. Areshkrishna Datta, Abdelhak Djouadi, Monoranjan Guchait, and Filip Moortgat. Detection of MSSM Higgs bosons from supersymmetric particle cascade decays at the LHC. *Nucl. Phys.*, B681:31–64, 2004.
22. Priyotosh Bandyopadhyay, Aresh Krishna Datta, and Biswarup Mukhopadhyaya. Signatures of gaugino mass non-universality in cascade Higgs production at the LHC. 2008. arXiv:0806.2367.
23. F. Moortgat, P. Olbrechts, and L. Pape. Search for a light Higgs boson in SUSY cascades. *CMS Note 2006/090*.
24. D. N. Spergel et al. First year wilkinson microwave anisotropy probe (WMAP) observations: Determination of cosmological parameters. *Astrophys. J. Suppl.*, 148:175, 2003.
25. D. N. Spergel et al. Wilkinson Microwave Anisotropy Probe (WMAP) three year results: Implications for cosmology. *Astrophys. J. Suppl.*, 170:377, 2007.
26. B. C. Allanach. SOFTSUSY: A C++ program for calculating supersymmetric spectra. *Comput. Phys. Commun.*, 143:305–331, 2002.
27. G. Belanger, F. Boudjema, A. Pukhov, and A. Semenov. micrOMEGAs: A program for calculating the relic density in the MSSM. *Comput. Phys. Commun.*, 149:103–120, 2002.
28. G. Belanger, F. Boudjema, A. Pukhov, and A. Semenov. micrOMEGAs: Version 1.3. *Comput. Phys. Commun.*, 174:577–604, 2006.
29. G. Belanger, F. Boudjema, A. Pukhov, and A. Semenov. micrOMEGAs2.0: A program to calculate the relic density of dark matter in a generic model. *Comput. Phys. Commun.*, 176:367–382, 2007.
30. Search for charged Higgs bosons: Preliminary combined results using LEP data collected at energies up to 209-GeV. 2001. hep-ex/0107031.
31. Pran Nath and R. Arnowitt.  $b$  to  $s$  gamma decay in supergravity grand unification and dark matter. *Phys. Lett.*, B336:395–401, 1994.
32. Pran Nath and R. Arnowitt. Event rates in dark matter detectors for neutralinos including constraints from the  $b$  to  $s$  gamma decay. *Phys. Rev. Lett.*, 74:4592–4595, 1995.
33. Howard Baer, Michal Brhlik, Diego Castano, and Xerxes Tata.  $b \rightarrow s\gamma$  constraints on the minimal supergravity model with large  $\tan(\beta)$ . *Phys. Rev.*, D58:015007, 1998.
34. Marcela Carena, David Garcia, Ulrich Nierste, and Carlos E. M. Wagner.  $b \rightarrow s\gamma$  and supersymmetry with large  $\tan(\beta)$ . *Phys. Lett.*, B499:141–146, 2001.
35. G. Degrandi, P. Gambino, and G. F. Giudice.  $B$  to  $X/s$  gamma in supersymmetry: Large contributions beyond the leading order. *JHEP*, 12:009, 2000.
36. E. Barberio et al. Averages of  $b$ -hadron properties at the end of 2006. 2007. arXiv:0704.3575.
37. Kwok Lung Chan, Utpal Chattopadhyay, and Pran Nath. Naturalness, weak scale supersymmetry and the prospect for the observation of supersymmetry at the tevatron and at the LHC. *Phys. Rev.*, D58:096004, 1998.
38. Jonathan L. Feng, Konstantin T. Matchev, and Takeo Moroi. Multi-teV scalars are natural in minimal supergravity. *Phys. Rev. Lett.*, 84:2322–2325, 2000.
39. Howard Baer, Tadas Krupovnickas, Stefano Profumo, and Piero Ullio. Model independent approach to focus point supersymmetry: From dark matter to collider searches. *JHEP*, 10:020, 2005.
40. W. Beenakker, R. Hopker, M. Spira, and P. M. Zerwas. Squark and gluino production at hadron colliders. *Nucl. Phys.*, B492:51–103, 1997.
41. M. Muhlleitner, A. Djouadi, and Y. Mambrini. SDECAY: A fortran code for the decays of the supersymmetric particles in the MSSM. *Comput. Phys. Commun.*, 168:46–70, 2005.
42. A. Djouadi, J. Kalinowski, and M. Spira. HDECAY: A program for Higgs boson decays in the standard model and its supersymmetric extension. *Comput. Phys. Commun.*, 108:56–74, 1998.
43. Abdelhak Djouadi, Jean-Loic Kneur, and Gilbert Moul-taka. SuSpect: A fortran code for the supersymmetric and Higgs particle spectrum in the MSSM. *Comput. Phys. Commun.*, 176:426–455, 2007.

44. CMS PRS, <http://cmsdoc.cern.ch/cms/PRS/results/susybsm/rep24/rep24.html>. *Search for Higgs Bosons in SUSY Cascades in CMS and Dark Matter with Non-universal Gaugino Masses*, 2008. Accessed 12 August, 2008.
45. T Sjostrand, L Lonnblad, S Mrenna, and P Skands. Pythia 6.3 physics and manual. *LU TP*, 03-38, 2003. hep-ph/0308153.
46. H. L. Lai et al. Global QCD analysis of parton structure of the nucleon: CTEQ5 parton distributions. *Eur. Phys. J.*, C12:375–392, 2000.
47. Veikko Karimaki. CMSIM, CMS simulation and reconstruction package. Site located at <http://cmsdoc.cern.ch/cmsim/cmsim.html>.
48. CMS physics technical design report. *CERN/LHCC 2006-001*, CMS TDR 8.1, 2006.
49. M.L. Mangano, M. Moretti, F. Piccinini, R. Pittau, and A.D. Polosa. Alpgen, a generator for hard multiparton processes in hard collisions. *JHEP*, 001:35, 2003.
50. CMS physics technical design report. *CERN/LHCC 2006-002*, CMS TDR 8.2, 2006.
51. CMS OO reconstruction. FAMOS: CMS Reconstruction Package. Site located at <http://cmsdoc.cern.ch/famos>.
52. CMS OO reconstruction. ORCA: CMS Reconstruction Package. Site located at <http://cmsdoc.cern.ch/orca>.
53. C Weiser. A combined secondary vertex based b-tagging algorithm in CMS. *CMS Note 2006/014*.
54. The level-1 trigger. *CERN/LHCC 2000-038*, CMS TDR 6.1, 2000.
55. Data acquisition and high-level trigger. *CERN/LHCC 2002-26*, CMS TDR 6.2, 2002.
56. L. Pape and Filip Moortgat. Hemisphere algorithm for separation of SUSY cascade chains. *Physics meeting at CERN 10/04/2006*.
57. CMS Particle Flow Group. The CMS particle flow algorithm. *CMS Note*. (In preparation).